

# Efficient frequency upconversion for single photons at telecommunication wavelengths with chip-scale Ti-indiffused periodically-poled lithium niobate waveguides

Zhenda Xie<sup>1,2,\*</sup>, Kai-Hong Luo<sup>3</sup>, Nicolae C. Panoiu<sup>4</sup>, Harald Herrmann<sup>3</sup>, Christine Silberhorn<sup>3</sup>, and Chee Wei Wong<sup>1,2,\*</sup>

<sup>1</sup> *Optical Nanostructures Laboratory, Columbia University, New York, NY 10027*

<sup>2</sup> *Fang Lu Mesoscopic Optics and Quantum Electronics Laboratory, University of California, Los Angeles, CA 90095*

<sup>3</sup> *Integrated Quantum Optics, Applied Physics, University of Paderborn, Warburger Str. 100, D-33098, Paderborn, Germany*

<sup>4</sup> *Department of Electronic and Electrical Engineering, University College London, Torrington Place, London WC1E 7JE, United Kingdom*

Email: xiezhenda@ucla.edu; cheewei.wong@ucla.edu

**Abstract:** Frequency upconversion for single photons at telecommunication wavelengths is important to simultaneously meet the different wavelengths requirement for long-distance communications and quantum memories in a quantum nodal network. It also enables the detection for the telecommunication “flying qubit” photons with silicon-based efficient single photon detectors with low dark count rates. Here we demonstrate single-photon frequency upconversion using a low-loss titanium-infused periodically-poled lithium niobate waveguide, pumped with a readily-available erbium-doped fiber amplifier in the L-band. Internal and conversion efficiencies up to 84.4% and 49.9% respectively have been achieved. Dark count rates are suppressed down to 44 kHz at 13.9% end-to-end quantum efficiency (including full

conversion and detection), enabled by our long-wavelength pump configuration and narrow 3.5 GHz bandpass filtering.

In proposed quantum optical communication network architectures, nonclassical photon sources are at different wavelengths for a diversity of nodes and for qubit storage-versus-communication implementations. Two dominant wavelength ranges are: (1) the telecommunication wavelength with low absorption losses in optical fibers and. (2) the visible/near-IR wavelengths between 600 to 800 nm for quantum memories. While the single photons at telecom wavelength are beneficial for the long distance quantum key distribution [1-4], visible/near-IR wavelengths are more compatible with the quantum memories [5-9] and detection systems. Most quantum memories are based on photonic interactions with atomic transition, and require the narrowband input at visible/near-IR wavelengths. These wavelengths are also compatible with the sophisticated single photon detectors using silicone avalanche photo diodes (APD), where the performances are superior to the conventional telecom single photon detectors using InGaAs APDs with both higher quantum efficiency and lower dark count (DC) rate [10]. Single photon frequency upconversion has been proposed from telecom wavelength to visible/NIR wavelengths as an efficient way to connect all the different devices working at different wavelengths [11]. It can be achieved by the sum-frequency generation (SFG) using a strong pump in a nonlinear optical medium [12-26]. Two approaches have been developed for the SFG: the first one uses a bulk period poled lithium niobate (PPLN) crystal with cavity enhancement [12-16] while the second one utilizes the reverse-proton-exchanged (RPE) PPLN waveguide [17-20]. Both schemes can achieve high conversion efficiency but the later one requires much lower pump power and is compatible for future integrated quantum circuit as a waveguide device. However, the RPE PPLN waveguide only support TM mode, which limits the polarization of the single photons on the waveguide chip. On the other hand, the titanium-infused (Ti:) PPLN waveguide [27] supports both TE and TM modes [28-31], which may be a more ideal choice for future photonic integration involving polarization degree of freedom. For

frequency upconversion at the single photon level, the photon leakage from the strong pump may greatly increase the DC rate and reduce the signal to noise ratio, as schematically shown in Fig. 1(a). This leakage may be resulted from the Raman scattering and cascaded nonlinear parametric processes [19, 20]. Because of its broadband feature, previous studies show that the DC rate can be reduced by narrowband spectral filtering [18]. Very low DC rate has been achieved using monochromator but overall quantum efficiency is also significantly reduced because of the high insertion loss of the monochromator. It also appears to be beneficial to have pump wavelength longer than the input signal, because of the much lower probability of anti-Stokes emission than the Stokes [19, 20]. However, for C-band input, special long-wavelength pump light sources through optical parametric oscillator was specially prepared [19].

Here we present the first experiment on the single photon frequency upconversion from telecom wavelength to visible/NIR wavelength, using a 35 mm-long Ti:PPLN waveguide, with a commercial-available L-band pump tunable laser and erbium-doped fiber amplifier (EDFA) at 1570 nm. For the 1542.3 nm to 778 nm upconversion, internal and conversion efficiencies of up to 84.4% and 49.9% are measured. Efficient narrow band filtering has been achieved down to 3.5 GHz to maximize the signal-to-noise ratio, which is compatible for quantum memory application with typical bandwidth on the level of tens of MHz. When tested with a single photon detector based on silicon APD, the DC rate can be suppressed to 44 kHz at 13.9% overall quantum efficiency.

The Ti:PPLN waveguide we use has a poling period of 17.90  $\mu\text{m}$  and a total length of 35 mm. Fig. 1(b) shows the microscope image of the waveguide. We have measured the propagation loss of the waveguide by monitoring the interference fringes of the low Q cavity caused by the Fresnel reflection on its two facets [32]. It has been done by scanning a 1550 nm tunable laser over the resonances. The propagation loss can be calculated to be 0.06 dB/cm, or 4.7% loss for a single pass through the waveguide. After this measurement, the input facet is anti-reflection (AR) coated with over 98% transmission from 1500 to 1700 nm, while the output

facet is anti-reflection (AR) coated with over 98% transmission from 750 to 850 nm. Our setup can be schematically shown in Fig. 1(c). The pump light comes from a tunable diode laser (Santec TSL-510) with its wavelength fixed at 1570 nm. It is amplified by an L-band EDFA (Manlight HWT-EDFA-B-L-PM-33-1-FC/APC) to a maximum power of 2 W. A Glan laser prism is used to ensure the pump is TM polarized before entering the Ti:PPLN waveguide. Fiber polarization controller is used to change the input power. Two narrow band interference filters (Semrock NIR01-1570/3-25) are cascaded to clean the pump light, with over 120 dB rejection for the amplified spontaneous emission noise from the EDFA. The pump beam is combined with the input signal on a dichroic mirror (DM1) before focusing into the Ti:PPLN waveguide. The single-photon signal is simulated by a weak coherent light source, which is from another tunable diode laser with tuning range from 1480 nm to 1580 nm (Ando AQ4321A). Two variable optical attenuators are connected in series to achieve over 120 dB attenuation for the laser beam down to single photon level. The Ti:PPLN waveguide is temperature stabilized in a homebuilt oven with an accuracy of 10 mK. The SFG output is separated by a long-pass filter from the pump and remaining input. After passing through the filtering system, it can be detected by a power meter or a single photon detection module (SPCM). The pump and remaining input is further separated by another dichroic mirror (DM2) and measured by two multi-mode-fiber coupled power meters respectively. The coupling efficiency for pump (from point 1 to point 3) and signal (from point 2 to point 4) beams is measured to be 33.0% and 33.3%, which is calculated to be 59.5% and 60.0% considering the reflection on the AR coatings at the output facet and the aspheric collimating lens at the output side (AL2).

We first characterize the phase matching of the Ti:PPLN waveguide. We find the frequency upconversion is most efficient while the SFG is in the  $TM_{01}$  mode [Fig. 2(a)], which may be a result of the mode overlapping inside the waveguide. At 30°C, the SFG power is measured as a function of the signal wavelength. The phase matching wavelength is 1514.8 nm and the full width half maximum is measured to be about 0.8 nm. The asymmetry of two satellite peaks may

be caused by the poling inhomogeneity. At the temperature of 130°C, we can shift the phase matching wavelength to the C-band at 1542.3 nm, as shown in Fig. 2(b). At both temperatures we measure the depletion efficiencies on port 4 while the input signal is fixed at 1514.8 nm and 1542.3 nm respectively with 100  $\mu$ W power, as shown in Fig. 3(a) and (b). At a coupled pump power of 780 mW, the maximum depletion efficiencies are measured to be 69.4% and 88.6% respectively, corresponding to internal conversion efficiencies of 66.1% and 84.4%. We also measure the SFG power at 130°C, as shown in Fig. 3(c). A maximum output power of 98.9  $\mu$ W is obtained, which corresponds to a maximum photon conversion efficiency of 49.9%. The DC rates are also measured with a fiber coupled SPCM (Perkin Elmer SPCM-AQRH-14), which is shown as the red curve in Fig. 3(a) and (b). A standard SMF-28 fiber is used for best coupling efficiency for the  $TM_{01}$  mode. Due to the high count rate, the saturation effect of the SPCM due to detector dead time give rises to a saturation of the measured photon count rate at high coupled pump powers. This is considered and the blue curves present corrected DC rates. The maximum DC rate at 130°C reaches 26.7 MHz, which is about 2.4 times of that at 30°C. This may be because of the higher anti-Stokes scattering rate at higher temperature and smaller wavelength separation from signal to pump. The DC rate measured here is much higher than the studies on RPE PPLN waveguide at similar conversion efficiencies but similar at comparable coupled pump powers. As the DC rate is mainly dependent only on pump power, we can expect similar performance if less pump is required. Here we use a relatively short waveguide of 35 mm and there may be some imperfections in the poling, as shown in the phase matching curve in Fig. 2(b). By increasing the length of the Ti:PPLN waveguide to 60 mm, the pump power can be reduced by a factor of 2.94, and it can be further reduced by improving the poling quality.

To describe the evolution of the mode amplitudes  $u_i$  upon mutual quasi-phase-matching interaction, we use the below system of equations for the SFG (denoted with subscript 3), signal (denoted with subscript 2), and pump (denoted with subscript 1) [33-35]:

$$i \frac{du_1}{dz} + \gamma_1 u_3 u_2^* e^{i\Delta\beta z} = 0, \quad (1a)$$

$$i \frac{du_2}{dz} + \gamma_2 u_3 u_1^* e^{i\Delta\beta z} = 0, \quad (1b)$$

$$i \frac{du_3}{dz} + \gamma_3 u_1 u_2 e^{-i\Delta\beta z} = 0, \quad (1c)$$

where  $u_1(z)$ ,  $u_2(z)$ , and  $u_3(z)$  are the mode amplitudes at the three frequencies and are measured in  $\sqrt{W}$ . The nonlinear parameters  $\gamma_i$  in the equations above are defined as:

$$\gamma_1 = \frac{\epsilon_0 \omega_1}{2\sqrt{P_1 P_2 P_3}} \int_{A_{nl}} dx dy \hat{\mathbf{e}}_1^*(x, y; \omega_1) \cdot \hat{\chi}_{eff}(\omega_3, -\omega_2) : \hat{\mathbf{e}}_2^*(x, y; \omega_2) \hat{\mathbf{e}}_3(x, y; \omega_3), \quad (2a)$$

$$\gamma_2 = \frac{\epsilon_0 \omega_2}{2\sqrt{P_1 P_2 P_3}} \int_{A_{nl}} dx dy \hat{\mathbf{e}}_1^*(x, y; \omega_1) \cdot \hat{\chi}_{eff}(\omega_3, -\omega_2) : \hat{\mathbf{e}}_2^*(x, y; \omega_2) \hat{\mathbf{e}}_3(x, y; \omega_3), \quad (2b)$$

$$\gamma_3 = \frac{\epsilon_0 \omega_3}{2\sqrt{P_1 P_2 P_3}} \int_{A_{nl}} dx dy \hat{\mathbf{e}}_1^*(x, y; \omega_1) \cdot \hat{\chi}_{eff}(\omega_3, -\omega_2) : \hat{\mathbf{e}}_2^*(x, y; \omega_2) \hat{\mathbf{e}}_3(x, y; \omega_3), \quad (2c)$$

where  $A_{nl}$  is the nonlinear modal area and  $\hat{\mathbf{e}}_i$  are the modal  $E$ -fields. In addition, the normalization powers,  $P_i$ , wave vector mismatch,  $\Delta\beta$ , and waveguide effective susceptibility are, respectively:

$$P_i = \frac{1}{4} \int_S [\hat{\mathbf{e}}_i(x, y) \times \hat{\mathbf{h}}_i^*(x, y) + \hat{\mathbf{e}}_i^*(x, y) \times \hat{\mathbf{h}}_i(x, y)] \cdot \hat{\mathbf{z}} dS, \quad i = 1, 2, 3, \quad (3a)$$

$$\Delta\beta = \beta(\omega_3) - \beta(\omega_1) - \beta(\omega_2) - \frac{2\pi}{\Lambda} = \beta_3 - \beta_1 - \beta_2 - \frac{2\pi}{\Lambda}, \quad (3b)$$

$$\hat{\chi}_{eff} = \frac{2}{\pi} \hat{\chi}. \quad (3c)$$

Here,  $\hat{\mathbf{h}}_i$  are the modal  $H$ -fields. The resulting SFG quasi-phase-matching bandwidth is given by [33]:

$$\delta\lambda = \frac{4\pi \cdot 0.4429}{L \left| \frac{\partial \Delta\beta}{\partial \lambda_2} \right|} = \frac{2 \cdot 0.4429 \lambda_2^2}{L |n_{g,2} - n_{g,3}|}, \quad (4)$$

where  $L$  is the length of the waveguide and  $n_g = c/v_g$  is the group index with  $v_g$  the group velocity.

Using the relation  $P_i = W_i v_{gi}$ , where  $W_i = \frac{1}{2} \int \epsilon(x, y) |\mathbf{e}_i(x, y)|^2 dx dy \equiv \frac{\epsilon_0 W_i}{2}$  is the mode energy per unit length, the nonlinear parameters  $\gamma_i$  can be expressed as:

$$\gamma_1 = \rho \omega_1 \int_{A_{nl}} dx dy \hat{\mathbf{e}}_1^*(x, y; \omega_1) \cdot \hat{\chi}_{eff}(\omega_3, -\omega_2) : \hat{\mathbf{e}}_2^*(x, y; \omega_2) \hat{\mathbf{e}}_3(x, y; \omega_3), \quad (5a)$$

$$\gamma_2 = \rho \omega_2 \int_{A_{nl}} dx dy \hat{\mathbf{e}}_2^*(x, y; \omega_2) \cdot \hat{\chi}_{eff}(\omega_3, -\omega_1) : \hat{\mathbf{e}}_1^*(x, y; \omega_1) \hat{\mathbf{e}}_3(x, y; \omega_3), \quad (5b)$$

$$\gamma_3 = \rho \omega_3 \int_{A_{nl}} dx dy \hat{\mathbf{e}}_3^*(x, y; \omega_3) \cdot \hat{\chi}_{eff}(\omega_1, \omega_2) : \hat{\mathbf{e}}_1(x, y; \omega_1) \hat{\mathbf{e}}_2(x, y; \omega_2). \quad (5c)$$

Here,  $\rho = \sqrt{\frac{2}{\epsilon_0 c^3} \frac{n_{g1} n_{g2} n_{g3}}{w_1 w_2 w_3}}$  is a frequency-independent coefficient. The resulting modeled SFG power versus pump power is shown in Fig. 3(d), with the power dependences versus waveguide distance shown in Fig. 3(d) inset. Without any fitting, the modeled SFG power is within the same order-of-magnitude and within 50% of the measured SFG power [Fig. 3(c)]. We also note that the numerical model does not incorporate single-photon detector saturation and hence for the power levels considered here the modelled SFG power is intrinsically linear with respect to pump power. At larger pump power, however, the theoretical model predicts a nonlinear dependence of SFG power on the pump power. In addition, the theory predicts a phase matching bandwidth of 0.65 nm, close to the experimental measurements.

In above measurements of Fig. 3, only a pair of cascaded interference filters is used, with an effective FWHM bandwidth of about 3 nm. As the photon leakage is broadband, any noise photon fall into this 3 nm bandwidth contribute as the dark count. We next reduce the filter bandwidth by using a high-efficiency ruled grating, as shown in Fig. 1(c). A double-pass configuration is used to reduce the filtering bandwidth down to 21.5 GHz. The transmission of this filtering system is measured to be 52.0%. This transmission is mainly limited by the grating efficiency of about 76%, and it may be further improved by optimizing the blaze angle. We perform the single photon upconversion test with an input photon flux at 1 MHz. The quantum efficiency and DC rate can be calculated by monitoring the upconversion counting rate from the SPCM, with results shown in Fig. 4. At 30°C, the maximum quantum efficiency is 15.6% with DC rate of 289 kHz; at 130°C, the maximum quantum efficiency is 19.5% with DC rate of 550 kHz. The DC rate is reduced by 16.9 dB with the double-pass grating filtering. We can further reduce the DC rate with even narrower filtering, by adding a fiber Fabry-Perot cavity (FFPC). The FFPC is formed on a 780 nm single mode fiber by two fiber Bragg gratings (FBG) with a separation of 820  $\mu\text{m}$ , which corresponds to a free spectral range (FSR) of 124 GHz. Together with the grating filter, only one transmission peak is selected. The two FBGs are made with

bandwidths of 2 nm and centered at 778 nm, which matches well with the SFG wavelength at 130°C. Both FBGs are made to be of 90% reflections, which result in a measured finesse of 36 and a transmission FWHM of 3.5 GHz. The peak transmission is measured to be 91%. As shown in Fig. 4(c), the DC rate can be suppressed by 27.8 dB to 44 kHz at a maximum quantum efficiency of 13.9%. The lower efficiency is mainly due to the mode mismatch between the 780 nm single mode fiber and  $TM_{01}$  mode for the SFG light from the Ti:PPLN waveguide. By optimizing the mode matching to SFG light with  $TM_{00}$  mode, higher single-mode-fiber coupling efficiency can be expected.

In conclusion, we demonstrate the single-photon-level frequency upconversion from telecom wavelength to NIR/visible wavelength using a Ti:PPLN waveguide. It is shown that the Ti:PPLN waveguide can realize the efficient frequency upconversion and this result may be important for the future integrated quantum circuit, because of its potential operation on the polarization degree of freedom. 84.4% internal and 49.9% conversion efficiencies have been achieved for the C-band input at 1542.3 nm. Efficient narrow band filtering down to 3.5 GHz has been realized by cascading a double-pass grating system and a FFPC, which greatly reduce the DC rate by 27.8 dB. After such filtering, a maximum quantum efficiency of 13.9% has been measured using a SPCM with 72% detection efficiency, and DC rate is as low as 44 kHz in this case. In this work the coupled pump power is about 800 mW to achieve high conversion efficiency, which is the main reason for the high DC rate without filtering. Improvement such as longer waveguide and better poling quality is under development. With the narrow band filtering technique we developed, the Ti:PPLN waveguide upconversion can be an ideal choice for the quantum memory systems and the efficient single photon detection for telecommunication wavelengths.

The authors acknowledge funding support from DARPA Defense Science Office under Dr. Prem Kumar with grant number D133-001-0076.

## References

1. C. Gobby, Z. L. Yuan, and A. J. Shields, Quantum key distribution over 122 km of standard telecom fiber. *Appl. Phys. Lett.* **84**, 3762 (2004).
2. P. Zhang, K. Aungskunsiri, E. Martín-López, J. Wabnig, M. Lobino, R. W. Nock, J. Munns, D. Bonneau, P. Jiang, H. W. Li, A. Laing, J. G. Rarity, A. O. Niskanen, M. G. Thompson, and J. L. O'Brien, Reference frame independent quantum key distribution server with telecom tether for on-chip client. *Phys. Rev. Lett.* **112**, 130501 (2014).
3. P. Jouguet, S. Kunz-Jacques, A. Leverrier, P. Grangier, and Eleni Diamanti, Experimental demonstration of long-distance continuous-variable quantum key distribution. *Nature Photon.* **7**, 378 (2012).
4. S. Wang, Chen, J.-F. Guo, Z.-Q. Yin, H.-W. Li, Z. Zhou, G.-C. Guo, and Z.-F. Han, 2 GHz clock quantum key distribution over 260 km of standard telecom fiber. *Opt. Lett.* **37**, 1008 (2012).
5. B. Julsgaard, J. Sherson, J. I. Cirac, J. Fiurax, and E. S. Polzik, Experimental demonstration of quantum memory for light. *Nature* **432**, 482 (2004).
6. W. Rosenfeld, S. Berner, J. Volz, M. Weber, and H. Weinfurter, Remote Preparation of an Atomic Quantum Memory. *Phys. Rev. Lett.* **98**, 050504 (2007).
7. G. Hetet, J. J. Longdell, A. L. Alexander, P. K. Lam, and M. J. Sellars, Electro-Optic Quantum Memory for Light Using Two-Level Atoms. *Phys. Rev. Lett.* **100**, 023601 (2008).
8. T. Chaneliere, D. N. Matsukevich, S. D. Jenkins, S. Y. Lan, T. A. B. Kennedy, and A. Kuzmich, Storage and retrieval of single photons transmitted between remote quantum memories. *Nature* **438**, 833 (2005).
9. K. S. Choi, H. Deng, J. Laurat, and H. J. Kimble, Mapping photonic entanglement into and out of a quantum memory. *Nature* **452**, 67 (2008).
10. R. H. Hadfield, Single-photon detectors for optical quantum information applications. *Nature Photon.* **3**, 696 (2009).

11. P. Kumar, Quantum frequency conversion. *Opt. Lett.* **15**, 1476 (1990).
12. M. A. Albota and F. N. C. Wong, Efficient single-photon counting at 1.55  $\mu\text{m}$  by means of frequency upconversion. *Opt. Lett.* **29**, 1449 (2004).
13. H. Pan, E. Wu, H. Dong, and H. Zeng, Single-photon frequency up-conversion with multimode pumping. *Phys. Rev. A* **77**, 033815 (2008).
14. H. Pan, H. Dong, H. Zeng, and W. Lu, Efficient single-photon counting at 1.55  $\mu\text{m}$  by intracavity frequency upconversion in a unidirectional ring laser. *Appl. Phys. Lett.* **89**, 191108 (2006).
15. H. Pan and H. Zeng, Efficient and stable single-photon counting at 1.55  $\mu\text{m}$  by intracavity frequency upconversion. *Opt. Lett.* **31**, 793 (2006).
16. C. E. Vollmer, C. Baune, A. Sambrowski, T. Eberle, V. Händchen, J. Fiurášek, and R. Schnabel, Quantum up-conversion of squeezed vacuum states from 1550 to 532 nm. *Phys. Rev. Lett.* **112**, 073602 (2014).
17. L. Ma, O. Slattery, and X. Tang, Single photon frequency up-conversion and its applications. *Phys. Rep.* **521**, 69 (2012).
18. L. Ma, J. C. Bienfang, O. Slattery, and X. Tang, Up-conversion single-photon detector using multi-wavelength sampling techniques. *Opt. Express* **19**, 5470 (2011).
19. J. S. Pelc, L. Ma, C. R. Phillips, Q. Zhang, C. Langrock, O. Slattery, X. Tang, and M. M. Fejer, Long-wavelength-pumped upconversion single-photon detector at 1550 nm: performance and noise analysis. *Opt. Express* **19**, 21445 (2011).
20. C. Langrock, E. Diamanti, R. V. Roussev, Y. Yamamoto, and M. M. Fejer, Highly efficient single-photon detection at communication wavelengths by use of upconversion in reverse-proton-exchanged periodically poled LiNbO<sub>3</sub> waveguides. *Opt. Lett.* **30**, 1725 (2006).
21. M. Rakher, L. Ma, O. Slattery, X. Tang, and K. Srinivasan, Quantum transduction of telecommunications-band single photons from a quantum dot by frequency upconversion. *Nature Photon.* **4**, 786 (2010).

22. N. K. Langford, S. Ramelow, R. Prevedel, W. J. Munro, G. J. Milburn, and A. Zeilinger, Efficient quantum computing using coherent photon conversion. *Nature* **478**, 360 (2011).
23. C. J. McKinstrie, M. Yu, M. G. Raymer, and S. Radic, Quantum noise properties of parametric processes. *Opt. Express* **13**, 4986 (2005).
24. D. Shayovitz, H. Herrmann, W. Sohler, R. Ricken, C. Silberhorn, and D. M. Marom, Time-to-space conversion of ultrafast waveforms at 1.55  $\mu\text{m}$  in a planar periodically poled lithium niobate waveguide. *Opt. Lett.* **38**, 4708 (2012).
25. M. Mohageg, A. B. Matsko, and L. Maleki, Lasing and up conversion from a nominally pure whispering gallery mode resonator. *Opt. Express* **20**, 16704 (2012).
26. Q. Zheng, H. Zhu, S.-C. Chen, C. Tang, E. Ma, and X. Chen, Frequency-upconverted stimulated emission by simultaneous five-photon absorption. *Nature Photon.* **7**, 234 (2013).
27. O. Kuzucu, F. N.C. Wong, S. Kurimura, and S. Tovstonog, Time-resolved single-photon detection by femtosecond upconversion. *Opt. Lett.* **33**, 2257 (2008).
28. H. Takesue, K. Inoue, O. Tadanaga, Y. Nishida, and M. Asobe, Generation of pulsed polarization-entangled photon pairs in a 1.55- $\mu\text{m}$  band with a periodically poled lithium niobate waveguide and an orthogonal polarization delay circuit. *Opt. Lett.* **30**, 293 (2005).
29. A. Martin, A. Issautier, H. Herrmann, W. Sohler, D. B. Ostrowsky, O. Alibart, and S. Tanzilli, A polarization entangled photon-pair source based on a type-II PPLN waveguide emitting at a telecom wavelength. *New J. Phys.* **12**, 103005 (2010).
30. G. Fujii, N. Namekata, M. Motoya, S. Kurimura, and S. Inoue, Bright narrowband source of photon pairs at optical telecommunication wavelengths using a type-II periodically poled lithium niobate waveguide. *Opt. Express* **15**, 12769 (2007).
31. K. H. Luo, H. Herrmann, S. Krapick, R. Ricken, V. Quiring, H. Suche, W. Sohler, C. Silberhorn, Two-color narrowband photon pair source with high brightness based on clustering in a monolithic waveguide resonator. arXiv: 1306.1756 (2013).

32. R. Regener and W. Sohler, Loss in low-finesse Ti:LiNbO<sub>3</sub> optical waveguide resonators. *Appl. Phys. B* **36**, 143 (1985).
33. M. M. Fejer, G. A. Magel, D. H. Jundt, and R. L. Byer, Quasi-phase-matched second harmonic generation: tuning and tolerances, *IEEE J. Quant. Elect.* **28**, 2631 (1992).
34. N. C. Panoiu, R. M. Osgood, and B. A. Malomed, Semidiscrete composite solitons in arrays of quadratically nonlinear waveguides, *Opt. Lett.* **31**, 1097 (2006).
35. N. C. Panoiu, B. A. Malomed, and R. M. Osgood, Semidiscrete solitons in arrayed waveguide structures with Kerr nonlinearity, *Phys. Rev. A.* **78**, 013801 (2008).

## Figures

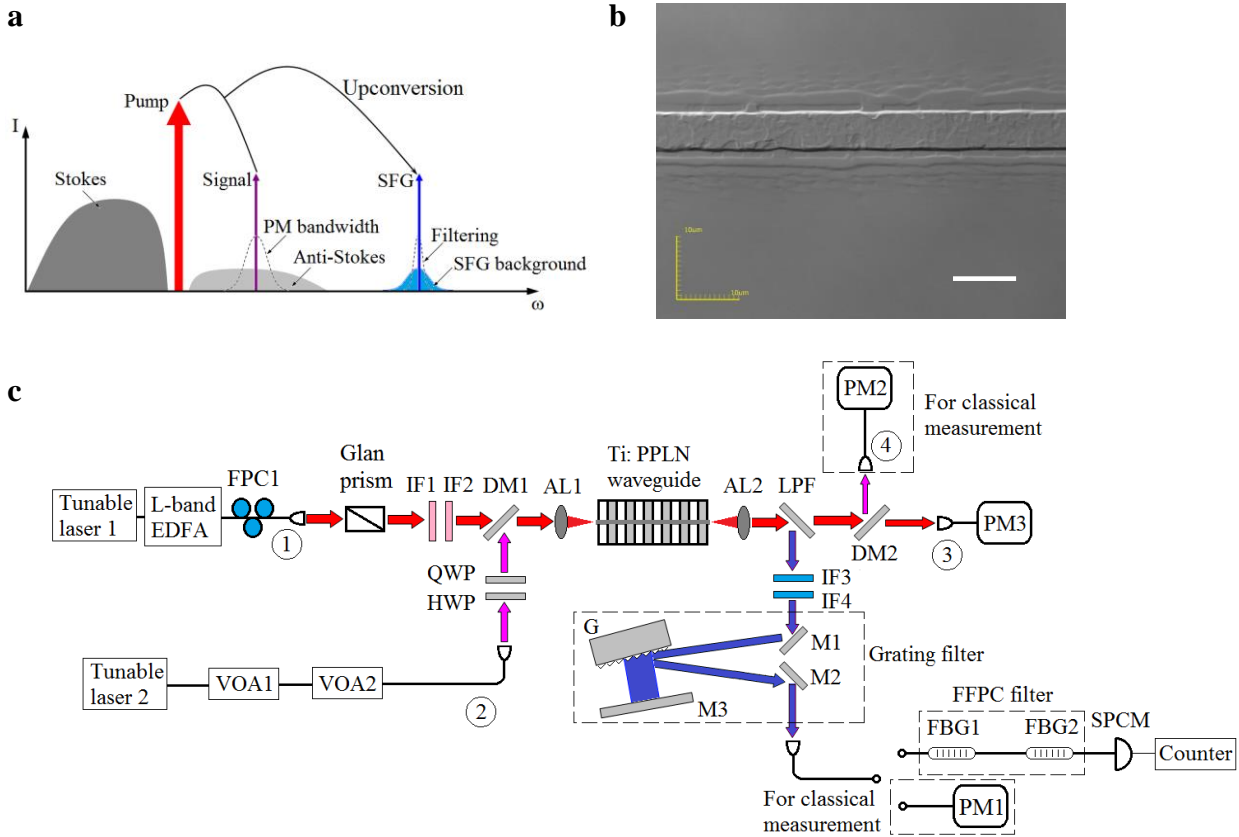


**Figure 1.** **a.** Schematic of the frequency upconversion. SFG background can be generated from the photon leakage of the strong pump light. The pump wavelength is set shorter than the signal wavelength for the relatively weaker anti-Stokes scattering. Photon leakage from within the phase matching bandwidth contributes as background noise, to be reduced by narrow band filtering. **b.** Microscope image of the PPLN waveguide chip. Scale bar: 10  $\mu\text{m}$ . **c.** Experiment setup. FPC: fiber polarization controller; IF: interference filter; DM: dichroic mirror; VOA: variable optical attenuator; HWP: half waveplate; QWP: quarter waveplate; AL: aspheric lens; LPF: long pass filter; M: mirror; G: ruled diffraction grating; PM: power meter; FPG: fiber Bragg grating; FFPC: fiber Fabry-Perot cavity; SPCM: single photon counting module. AL1 is AR coated for 1050 to 1620 nm and AL2 is AR coated for 650 to 1050 nm. Optical power can be measured at points 1, 2, 3 and 4 for the transmission test. The grating filter and FFPC filter can be inserted to reduce the DC rate.

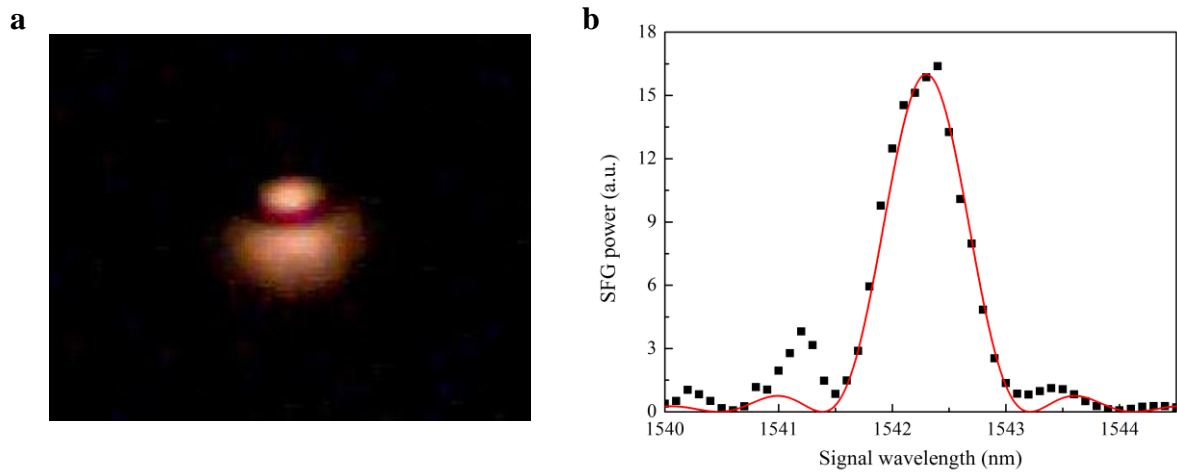


**Figure 2.** **a.** Far-field image of the  $TM_{01}$  mode. **b.** Wavelength tuning curve at  $130^\circ C$ . The dots show the experimental results, and the peak SFG conversion can be achieved at a phase matching wavelength of 1542.3 nm. The solid curve is a sinc square fit.

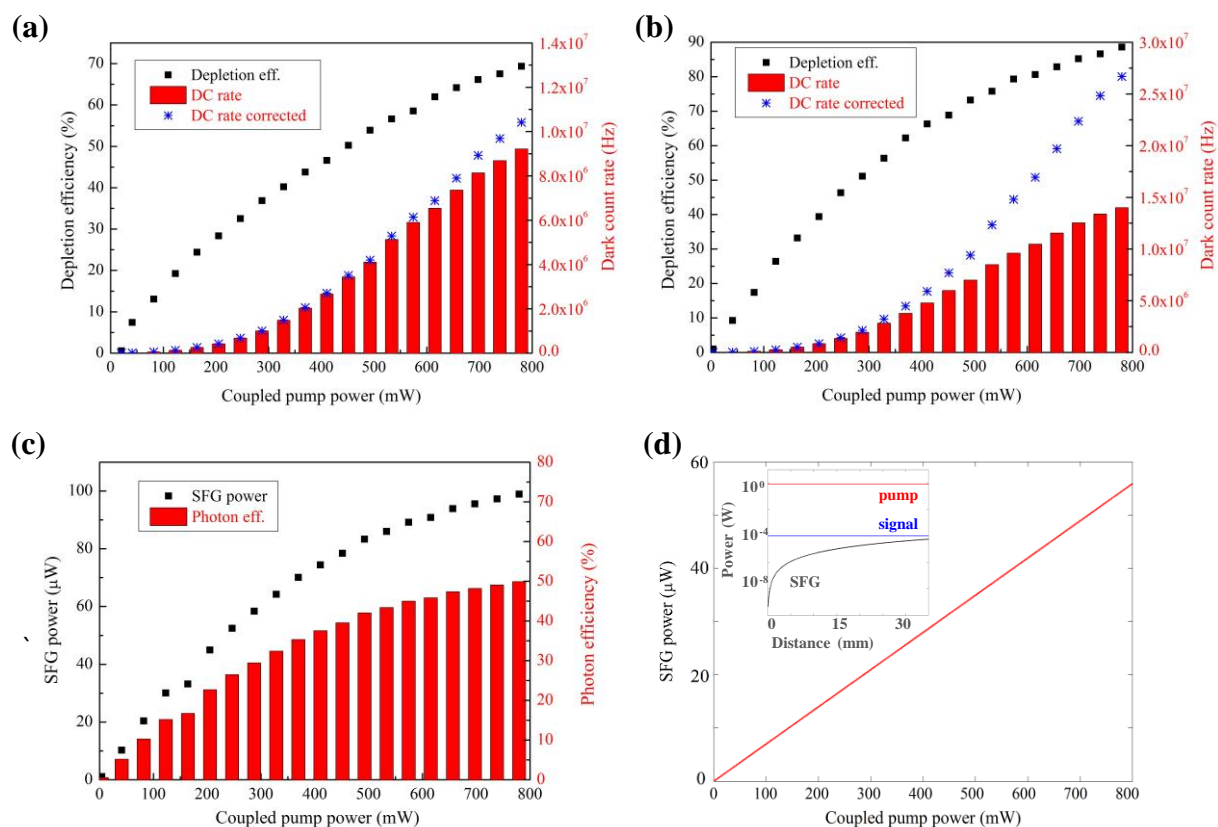


**Figure 3.** Conversion efficiency and DC rate. (a) Depletion efficiency and DC rate measured at 30°C. (b) Depletion efficiency and DC rate measured at 130°C. (c) SFG power and photon efficiency measured with 100  $\mu$ W signal input at 130°C. (d) Modeled SFG power versus coupled pump power. Inset: SFG, signal and pump powers versus distance at 800 mW pump power.

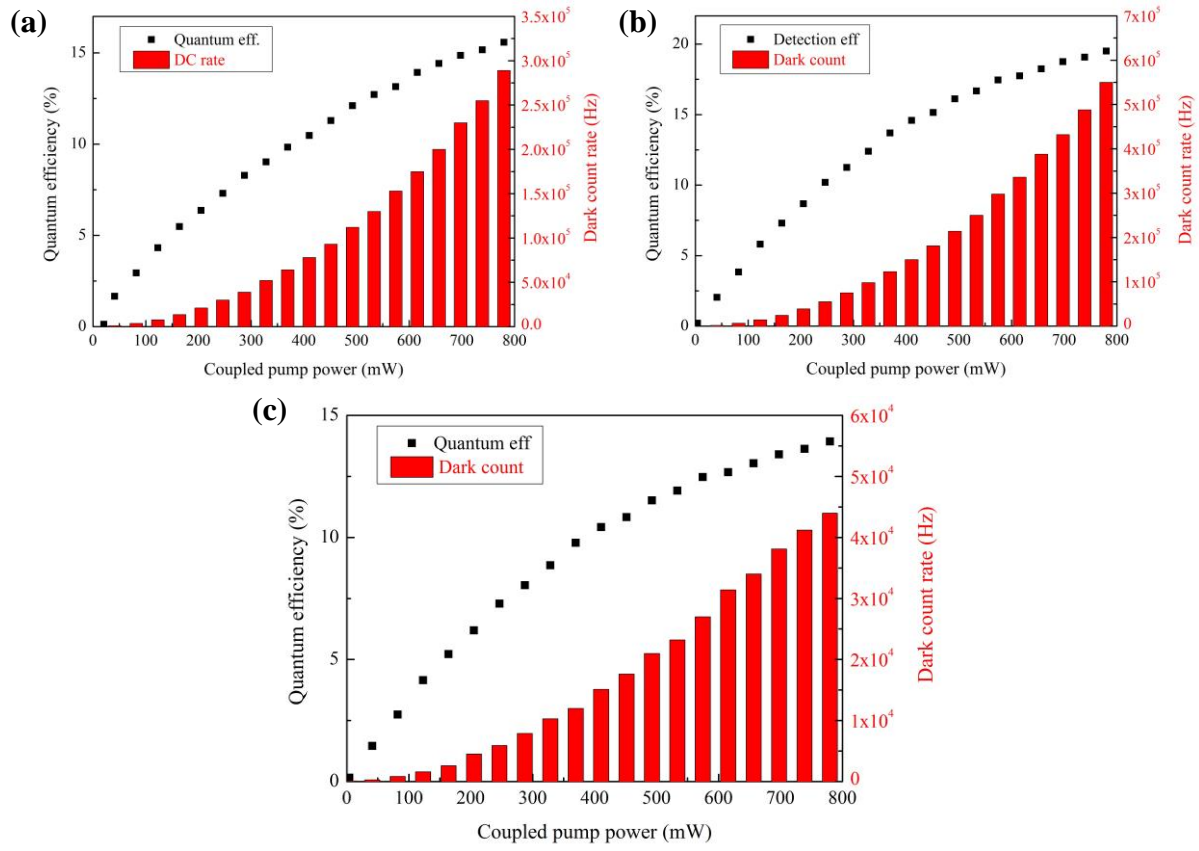


**Figure 4.** Quantum efficiency and DC rate measurement with grating and FFPC filters. (a) Quantum efficiency and DC rate measured with grating filter at 30°C. (b) Quantum efficiency and DC rate measured with grating filter at 130°C. (c) Quantum efficiency and DC rate measured with grating and FFPC filters at 130°C.